Journal of the European Ceramic Society **16** (1996) 1171–1178
Copyright © 1996 Elsevier Science Limited
Printed in Great Britain. All rights reserved
PII:S0955-2219(96)00048-9
0955-2219/96/$15.00

Sinterability of Spinel ($MgAl_2O_4$)-Zirconia Composite Powder Prepared by Double Nozzle Ultrasonic Spray Pyrolysis

Takayuki Suzuki, Kiyoshi Itatani,* Mamoru Aizawa, F. Scott Howell & Akira Kishioka

Department of Chemistry, Faculty of Science and Engineering, Sophia University, 7-1 Kioi-cho Chiyoda-ku, Tokyo 102, Japan

(Received 8 November 1995: revised version received 4 February 1996; accepted 20 February 1996)

Abstract

Two kinds of spinel ($MgAl_2O_4$)-zirconia (ZrO_2) composite powders were prepared by double nozzle ultrasonic spray pyrolysis; the aqueous solutions in the $Mg(NO_3)_2$-$Al(NO_3)_3$ and $ZrOCl_2$-YCl_3 systems were spray-pyrolysed in a hot zone of an electric furnace heated at 900°C, using two ultrasonic vibrators. The compositions of the composite powders were as follows: (1) Sample No. 1: $MgAl_2O_4$ 93·36 mol% and yttria-stabilized tetragonal ZrO_2 polycrystals (Y-TZP) 6·64 mol% and (2) Sample No. 2: $MgAl_2O_4$ 75·51 mol% and Y-TZP 24·49 mol%. While $MgAl_2O_4$ and Y-TZP were present in both powders, MgO was additionally detected from Sample No. 2; such MgO disappeared when it was heated up to 1100°C or higher. The composite powders contained spherical particles with diameters of below 2 μm and, in part, acicular particles with long axis lengths of 1 to 2 μm. The wet-milled powder of Sample No. 1 showed an excellent sinterability; when the composite powder compact was fired at 1700°C for 10 h, the relative density attained 97·6%. Copyright © 1996 Elsevier Science Ltd

1 Introduction

Since spinel ($MgAl_2O_4$) ceramic has a high melting point (2105°C) and excellent resistance to acid and alkali, a large amount of $MgAl_2O_4$ ceramics is now used as a refractory for furnace walls and firebricks.[1–3] Attention has also been directed toward the application of $MgAl_2O_4$ ceramics to humidity sensors.[4–6] Except for these practical and potential uses, the application of $MgAl_2O_4$ to other fields has been restricted, chiefly due to the insufficient mechanical strength at room and high temperatures.[7] In order to improve the mechanical strength of $MgAl_2O_4$ ceramics, many researchers investigated the fabrication of (i) dense ceramics and/or (ii) composites with other materials.[8] Dense $MgAl_2O_4$ ceramics may be fabricated using powders with primary particle sizes of ≤ 200 nm prepared by various advanced techniques: coprecipitation,[9] vapour-phase oxidation,[10] spray pyrolysis,[11] freeze drying[12] and sol-gel techniques.[13] The composites of $MgAl_2O_4$ with ZrO_2 are expected to enhance the mechanical strength, because Fujita *et al.*[8] demonstrated that the maximum fracture toughness (K_{IC}) is 6·3 MPa $m^{1/2}$ and the bending strength of ZrO_2-dispersed MgO-Al_2O_3 ceramics attains 400 MPa. Nevertheless, no information on ZrO_2-dispersed stoichiometric $MgAl_2O_4$ ceramics has been available.

The authors prepared various calcium phosphate powders by spray pyrolysis;[14–16] this technique has the advantages of preparing the powders with (i) submicrometer-sized primary particles, (ii) narrow particle size distribution and (iii) homogeneous composition.[17] Nevertheless, conventional spray pyrolysis is not always suitable for the preparation of composite powders containing two or more compounds, partly because it is difficult to prepare a solution containing such multicomponent ions without precipitation, and partly because the difference in solubility among metal salts in the starting solution often causes compositional inhomogeneity in the spray-pyrolysed powder.[17] In order to prepare ZrO_2-dispersed stoichiometric $MgAl_2O_4$ without a mixing operation, we assembled a novel spray pyrolysis apparatus using two ultrasonic vibrators. By using this apparatus, we examined (i) the preparation conditions of ZrO_2-dispersed stoichiometric $MgAl_2O_4$ powders and (ii) the sinterabilities of the resulting composite powders.

*To whom correspondence should be addressed.

2 Experimental Procedure

2.1 Preparation of composite powders

Figure 1 shows the schematic diagram of the reaction apparatus. This apparatus was composed of (I) a spraying zone, (II) a heating zone and (III) a powder collecting zone. Each zone will be explained below.

(I) Spraying zone

The preparation conditions of the starting solutions are shown in Table 1. The starting solutions for $MgAl_2O_4$ and Y-TZP were prepared as follows: (i) the desired concentrations of $Mg(NO_3)_2 \cdot 6H_2O$ and $Al(NO_3)_3 \cdot 9H_2O$ were dissolved in deionized water to form the solutions for preparing $MgAl_2O_4$; (ii) the desired concentrations of $ZrOCl_2 \cdot 8H_2O$ and $YCl_3 \cdot 6H_2O$ with Y/(Zr+Y) = 0·03 were dissolved in deionized water to form the solutions for preparing Y-TZP. The droplets were formed using ultrasonic vibrators (a).

(II) Heating zone

The droplets were introduced into the mullite tube (e), heated by an electric furnace (d) using a carrier gas: Ar gas (b) for preparing $MgAl_2O_4$ and O_2 gas (c) for preparing ZrO_2. The spray pyrolysis was carried out at 900°C. The temperature was recorded using thermocouples (f).

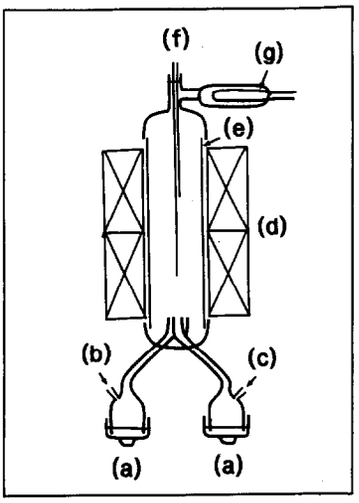

Fig. 1. Schematic diagram of the reaction apparatus. (a) Ultrasonic vibrator, (b) Ar carrier gas, (c) O_2 carrier gas, (d) Electric furnaces (length: 600 mm), (e) Mullite tube (diameter: 60 mm), (f) Thermocouple (Pt-Pt· 13% Rh), (g) Test-tube type filter.

(III) Powder collecting zone

The resulting powder was collected by a test-tube type filter (g); the gas formed by the spray pyrolysis was inhaled by an aspirator.

2.2 Calculation of the mean diameter of droplets

The mean diameter of the droplets ($\bar{d}$) was determined by the following equation:[18]

$$\bar{d} = 0{\cdot}34\left(\frac{8\pi\sigma}{\rho f^2}\right)^{\frac{1}{3}} \quad (1)$$

where σ is the surface tension of the solution, ρ is the density of the solution, and f is the frequency (= 2·4 MHz) of the ultrasonic vibrator.

2.3 Sintering of composite powders

A part of the resulting powder was wet-milled using a zirconia mortar and pestle in the presence of acetone. The as-prepared and wet-milled powders were uniaxially pressed at 120 MPa in steel dies to form cylindrical compacts with diameters of 10 mm and thickness of ~2 mm; then the compacts were cold-isostatically pressed at 150 MPa. The compacts were heated in an electric furnace (heating elements: $MoSi_2$) at a temperature between 1400°C and 1700°C for 10 h in air. The heating rate from room temperature up to the desired temperatures was 10°C min^{-1}. The bulk densities of the green and sintered compacts were calculated on the basis of the weights and dimensions. The relative density was calculated by dividing the bulk density by the true density measured picnometrically.

2.4 Evaluations of resulting powders and sintered compacts

The crystalline phases of the resulting powders and sintered compacts were examined using an X-ray diffractometer (XRD; 40 kV, 25 mA; Model RAD-IIA, Rigaku, Tokyo) with Ni-filtered CuKα radiation and a Fourier-transform infrared spectrophotometer (FT- IR; Model 8600PC, Shimadzu, Kyoto). The quantitative analyses of the powders were conducted using an X-ray fluorescence apparatus (XRF; Model SXF1200, Shimadzu, Kyoto).

The specific surface areas of the powders were measured by a Brunauer-Emmett-Teller (BET) technique, using nitrogen (N_2) as an adsorption gas. The true densities of the powders were mea-

Table 1 Preparation conditions of starting solutions

Sample No.	Spray I			Spray II		
	$Mg(NO_3)_2$ mol dm^{-3}	$Al(NO_3)_3$ mol dm^{-3}	Ar flow rate dm^3 min^{-1}	$ZrOCl_2$ mol dm^{-3}	YCl_3 mol dm^{-3}	O_2 flow rate dm^3 min^{-1}
1	$2{\cdot}0 \times 10^{-1}$	$4{\cdot}0 \times 10^{-1}$	820	$9{\cdot}7 \times 10^{-2}$	$3{\cdot}0 \times 10^{-3}$	400
2	$2{\cdot}0 \times 10^{-1}$	$4{\cdot}0 \times 10^{-1}$	820	$9{\cdot}7 \times 10^{-2}$	$3{\cdot}0 \times 10^{-3}$	800

sured picnometrically at 25°C. The agglomerate strengths were examined from the data on the relationship between relative densities of the compacts and compressed pressures.

The particle shapes of the powders were observed using a transmission electron microscope (TEM; Model H-9000, Hitachi, Tokyo), while the microstructures of the sintered compacts were observed using a scanning electron microscope (SEM; Model S-430, Hitachi, Tokyo). The dispersion states of elements in the sintered compacts were examined using an energy-dispersive X-ray analyser (EDX; Model EMAX-1500, Horiba, Kyoto). The crystal system of ZrO_2 in the sintered compacts was examined using a Raman spectroscope (Ar laser tuned to 514·5 nm).

3 Results and Discussion

3.1 Preparation of $MgAl_2O_4$-ZrO_2 composite powders

3.1.1 Crystalline phases of the resulting powders

Figure 2 shows the XRD patterns of the resulting powders. While $MgAl_2O_4$[19] and t-ZrO_2 (yttria-stabilized ZrO_2 polycrystals: Y-TZP)[20] were present in both powders, MgO[21] was additionally detected from Sample No. 2. The X-ray intensities of Y-TZP in Sample No. 2 were higher than those in Sample No. 1.

The compositions of the powders heat-treated at 1400°C were examined using XRF. The composition of Sample No. 1 was: $MgAl_2O_4$, 93·36 mol% and Y-TZP, 6·64 mol%, whereas that of Sample No. 2 was: $MgAl_2O_4$, 75·51 mol% and Y-TZP, 24·49 mol%. Hereafter, Samples No. 1 and 2 are designated as MZ(6·64) and MZ(24·49), respectively. The numbers in parentheses indicate the Y-TZP content.

As shown above, the Y-TZP content in MZ(24·49) powder is higher than that in MZ(6·64) powder, when the flow rate of O_2 gas for preparing Y-TZP is enhanced from 150 to 800 cm^3 min^{-1}. It should be noted that the Y-TZP content is controlled by changing the flow rate of O_2 gas. Regardless of the $MgAl_2O_4$ contents being higher than Y-TZP contents in MZ(6·64) and MZ(24·49) powders, however, X-ray intensities of $MgAl_2O_4$ are lower than those of Y-TZP. Since MgO was detected from MZ(24·49), this phenomenon is explained by assuming that the crystal growth of $MgAl_2O_4$ is inhibited by the sluggish reaction between MgO and Al_2O_3.

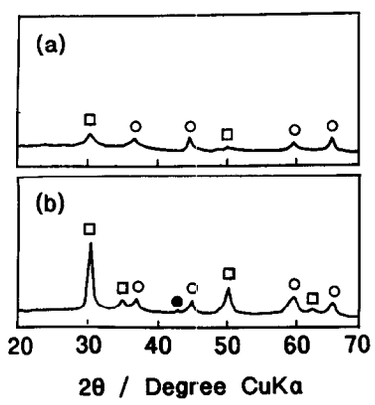

Fig. 2. XRD patterns of the resulting powders. (a) Sample No. 1, (b) Sample No. 2; ○: $MgAl_2O_4$, □: t-ZrO_2, ●: MgO.

The residence time of the droplets in the present furnace is estimated to be only ~40 s; thus it is probable that the spray-pyrolysed powders contain unreacted materials and adsorbed water. FT-IR analysis was conducted to elucidate whether these materials were included in the powders or not. Results are shown in Fig. 3. In MZ(6·64) and MZ(24·49) powders, the broad absorption bands appeared in the range of 2700 to 3650 cm^{-1}, whereas the absorption peaks appeared in the range of 1300 to 1700 cm^{-1}. The absorption peaks in the range of 1300 to 1700 cm^{-1} may be assigned to the NO_3^- and the band in the range of 2700 to 3650 cm^{-1} to the H_2O stretching vibration.[22]

The powder appears to be formed via the following spray-pyrolysis routes: (i) the evaporation of solvent (water), (ii) the pyrolysis of the precipitated metal salts, and (iii) the solid-state reactions of the metal salts/metal oxide. Since four kinds of starting materials are employed in the present experiment, the spray pyrolysis process seems to be quite complex; but it probably includes the pyrolysis of each starting material.

$$Mg(NO_3)_2{\cdot}6H_2O \xrightarrow{95°C} \text{melt} \xrightarrow{250°C}$$
$$2MgO{\cdot}Mg(NO_3)_2{\cdot}5H_2O \xrightarrow{430°C} MgO \quad (2)[23]$$

$$Al(NO_3)_3{\cdot}9H_2O \xrightarrow{73°C} \text{melt} \xrightarrow{140°C}$$
$$4Al_2O_3{\cdot}3N_2O_5{\cdot}14H_2O \xrightarrow{200°C} Al_2O_3 \quad (3)[24]$$

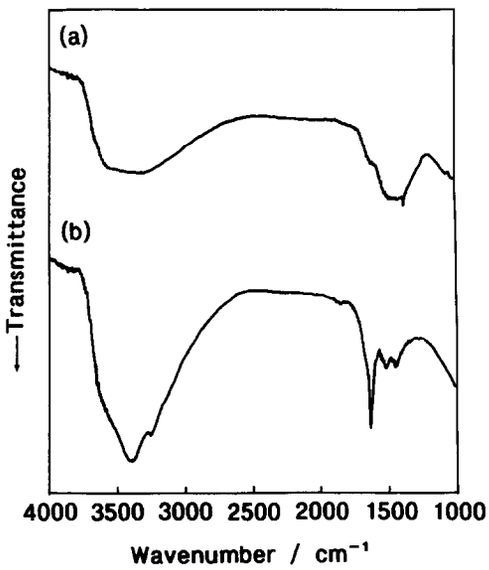

Fig. 3. FT-IR spectra of the resulting powders. (a) MZ(6.64) powder and (b) MZ(24.49) powder.

The reaction of MgO with Al_2O_3 may participate in the formation of $MgAl_2O_4$, because MgO was detected from MZ(24.49) powder.

$$MgO + Al_2O_3 \rightarrow MgAl_2O_4 \quad (4)$$

The FT-IR results indicate that NO_3^- and H_2O are present in MZ(6·64) and MZ(24·49) powders; these materials which are released by the pyrolysis of magnesium and aluminium salts are adsorbed on the resulting powders.

On the other hand, the thermal decompositions of zirconium and yttrium salts ($ZrOCl_2 \cdot 8H_2O$ and $YCl_3 \cdot 6H_2O$) may occur via the following routes:

$$ZrOCl_2 \cdot 8H_2O \xrightarrow{150°C} ZrOCl_2 \cdot 2H_2O \xrightarrow{210°C} ZrOCl_2 \xrightarrow{410°C} ZrO_2 \quad (5)[25]$$

$$YCl_3 \cdot 6H_2O \xrightarrow{\sim 240°C} YCl_3 \xrightarrow{715°C} YOCl \xrightarrow{1000°C} Y_2O_3 \quad (6)[26]$$

The resulting Y_2O_3 must be solid-dissolved into ZrO_2, because Y-TZP was detected by XRD.

3.1.2 Powder properties

Figure 4 shows the TEM micrographs and particle size distributions of the resulting powders. The solid spherical particles, hollow spherical particles, fragments of spherical particles and needle-like particles were present in MZ(6.64) powder (Fig. 4(a)). Most of the diameters of the spherical particles ranged from 0·1 to 1·4 μm (Fig. 4(a')). Although the long-axis lengths of the acicular particles are not plotted in the figure, they ranged from 1 to 2 μm. The particle shapes of MZ(24·49) powder (Fig. 4(b)) were similar to those of MZ(6·64) powder; however, the particle-size distribution width of MZ(24·49) powder (Fig. 4 (b')) was wider than that of MZ(6·64) powder.

Although the mean diameters of the droplets for preparing $MgAl_2O_4$ and Y-TZP are found from calculation to be 2·3 μm, the actual mean particle diameters are 0·47 and 0·60 μm, respectively; moreover, some spherical particles had diameters as large as ~1·5 μm. The spherical particles with diameters of ~0·5 μm are completely filled or 'solid'; however, the particles with diameters of ~1·5 μm appear to be 'hollow', because the insides of these large particles are translucent (see Fig. 4(b)). Such large particles may form when the coalesced droplets are spray-pyrolysed; the fragments are formed by the explosion of some spherical droplets/particles during the spray pyrolysis. It is noted that needle-like particles are present in the powder, although their formation route is unclear.

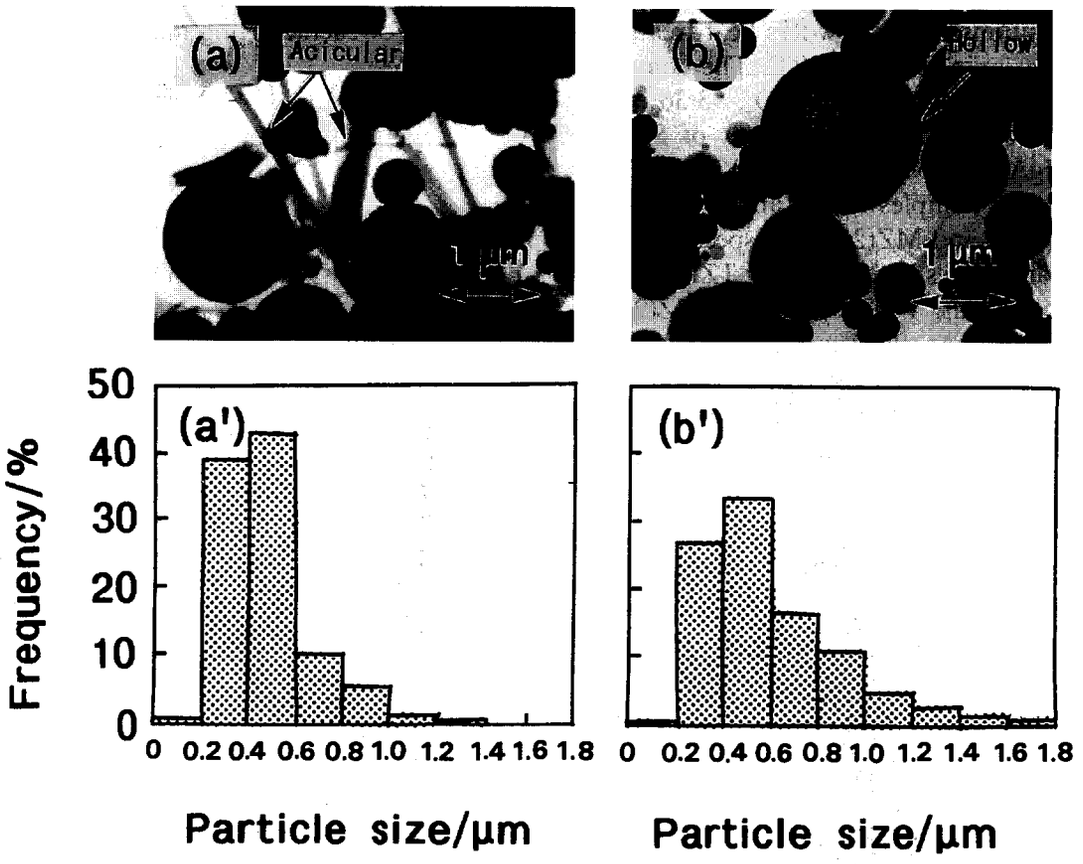

Fig. 4. TEM micrographs and secondary particle size distributions of the resulting powders. (a), (a'): TEM micrograph and secondary particle size distribution of MZ(6·64) powder; (b), (b'): TEM micrograph and secondary particle size distribution of MZ(24·49) powder.

The true densities of MZ(6·64) and MZ(24·49) powders were 3·68 and 4·36 g cm^{-3}, respectively. The density of MZ(24·49) powder is higher than that of MZ(6·64), reflecting the fact that the Y-TZP content is higher in the former than the latter. These densities are almost in accord with the theoretical densities calculated from their compositions.

The specific surface areas of MZ(6·64) and MZ(24·49) powders were 26·9 $m^2 g^{-1}$ and 14·9 $m^2 g^{-1}$, respectively. Since the Y-TZP content in MZ(24·49) powder is higher than that in MZ(6·64), the specific surface area appears to be reduced with Y-TZP content. This phenomenon is ascribed to more appreciable crystal growth of ZrO_2 than that of $MgAl_2O_4$ (see Fig. 2).

The sintering may be restricted when 'hard' agglomerates are present in the powder.[27] Thus the agglomerate strengths of the resulting powders were examined by plotting the relative densities against the compaction pressures. Results are shown in Fig. 5. The plots of the relative densities of MZ(6·64) powder compact against compaction pressures were expressed as two straight lines with the inflection point at ~90 MPa. The inflection point in the case of the wet-milled powder appeared at ~60 MPa; moreover, the relative densities of the wet-milled powder compacts were higher than those of the as-prepared powder compacts. The plots of the relative densities of MZ(24·49) powder compact against the compaction pressures were also expressed as two straight lines with one inflection point at ~110 MPa. The inflection point of the wet-milled powder compacts appeared at ~50 MPa; the relative densities of these compacts were higher than those without the milling operation.

The inflection point indicates the pressure at which the 'hard' agglomerates start to fracture; the fragments are rearranged into closer packing with higher compaction pressure.[28] When the relative densities of spray-pyrolysed ZrO_2 powder compacts were plotted against compaction pressures, one inflection point appeared at ~80 MPa. Similar results have been obtained by Haberko.[29] The pressures (~90 MPa) of the inflection points in the case of as-prepared powder compacts are almost in accord with those (~80 MPa) in the case of pure ZrO_2 powders, which suggests that most of the 'hard' agglomerates can be regarded as Y-TZP. These 'hard' agglomerates may be easily fractured into several pieces, because the inflection points in the case of wet-milled powder compacts appear at lower pressure than those in the case of as-prepared powder compacts.

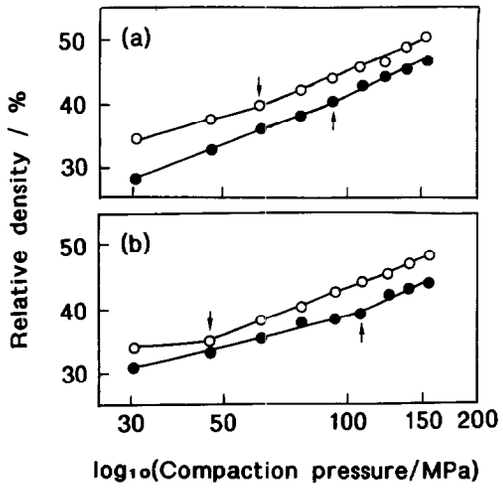

Fig. 5. Relationship between relative density of the compact and compaction pressure. (a) MZ(6·64), (b) MZ(24·49); ●: as-prepared powder compact, ○: wet-milled powder compact. Arrow marks indicate the inflection points.

3.1.3 Phase changes during heating of the resulting powders

The MZ(24·49) powder contains MgO, together with $MgAl_2O_4$ and Y-TZP. Thus it is important to determine whether or not MgO disappears during the heating of the resulting powder. First, DTA-TG measurements of the resulting powders were performed from room temperature up to 1400°C. Results are shown in Fig. 6. The DTA curve of MZ(6·64) (Fig. 6(a)) showed that the endothermic and exothermic effects started to appear at ~310°C and above 1270°C, respectively. Corresponding to these effects, the weight losses occurred stepwise in the ranges of 100–200°C, 200–400°C, 400–750°C and over 750°C. The DTA curve of MZ(24·49) (Fig.6 (b)) showed that the endothermic effects appeared at 66°C, 105°C, 160°C and 380°C. The weight losses occurred stepwise in the ranges of 50–150°C, 150–450°C and over 450°C.

The phase changes during heating of MZ(6·64) and MZ(24·49) powders were checked by X-ray

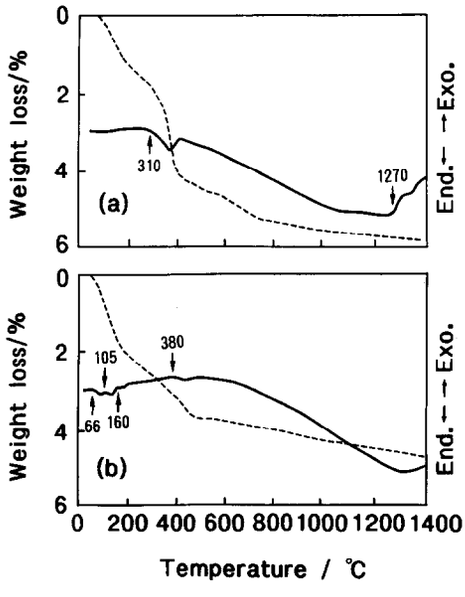

Fig. 6. DTA-TG curves of (a) MZ(6·64) powder and (b) MZ(24·49) powder. Heating rate: 10°C min^{-1}.

diffractometry. Results are shown in Fig. 7. In the case of MZ(6·64) powder, MgO was present in the temperature range of 300°C to 1100°C; the crystallinity of $MgAl_2O_4$ was enhanced above 1100°C. In the case of MZ(24·49) powder, the crystallinity of $MgAl_2O_4$ increased but that of ZrO_2 decreased slightly with temperature above 1000°C; MgO was present in the temperature range of 400°C to 1000°C.

The stepwise weight losses below 200°C indicate the releases of chemically and physically adsorbed water and of NO_3^- ions. On the other hand, the endothermic effects which start at 310°C in the case of MZ(6·64) powder and at 380°C in the case of MZ(24·49) powder are attributed to the formation of MgO. The crystallinity of $MgAl_2O_4$ increases with decreasing crystallinity of MgO at and above 1000~1100°C, which indicates that MgO reacts with Al_2O_3 to form $MgAl_2O_4$.

3.2 Sintering of $MgAl_2O_4$–Y-TZP powders

3.2.1 Effect of milling operation on sintering of the composite powders

Since the 'hard' agglomerates are included chiefly in the Y-TZP powder, the effects of milling operation on sintering of the powders are discussed in this section. Figure 8 shows the changes in relative density of the sintered compact with firing temperature from 1400°C to 1700°C. The relative density of MZ(6·64) compact was enhanced by the wet-milling operation; the maximum relative density attained 97.6% at 1700°C. Although the results for MZ(24·49) compact were similar to those for MZ(6·64) compact, the former relative densities were lower than the latter ones; moreover, the relative density of MZ(24·49) compact was reduced above 1600°C.

The above results reveal that the wet-milling operation is effective for enhancing the relative densities of the sintered compacts. This phenomenon may be ascribed to the decrease in the number of 'hard' agglomerates,[27] due to the milling operation (see Fig. 5). The effect of the milling operation on sintering of MZ(6·64) powder appears more appreciable than on that of MZ(24·49) powder, because the agglomerate strengths of MZ(6·64) powder seem to be lower than those of MZ(24·49) powder. Since the collapse of the hard agglomerates becomes difficult with Y-TZP content, the remaining 'hard' agglomerates in MZ(24·49) powder make their homogeneous packing difficult, thus retarding the densification. Moreover, the mass transfer of $MgAl_2O_4$ may be inhibited by Y-TZP. Details will be explained in the next section.

3.2.2 Microstructural evaluation of sintered compacts

Since the dense composite compact with the relative density of 97·6% could be fabricated at the firing temperature of 1700°C, the microstructure of this sintered MZ(6·64) compact was examined using SEM, XRD and Raman spectroscopy. Results are shown in Fig. 9. The SEM micrograph (Fig. 9(a)) showed that the large polyhedral grains with sizes of ~20 μm were packed closely: the small spherical grains with diameters of ~3 μm were present not only on grain boundaries but also inside the large grains. The XRD pattern (Fig. 9(b)) revealed that $MgAl_2O_4$ and t-ZrO_2 were detected from the sintered body. The Raman spectrum (Fig. 9(c)) showed that the crystal system of the ZrO_2 was assigned to be tetragonal.[30] These results indicate that ZrO_2 is stabilized by Y_2O_3 and that no reaction is observed between $MgAl_2O_4$ and Y-TZP.

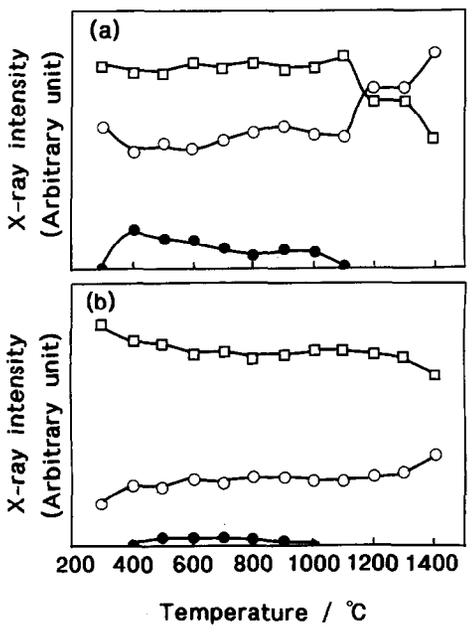

Fig. 7. Phase changes during the heating of (a) MZ(6·64) and (b) MZ(24·49); ○: $MgAl_2O_4$; (2θ = 36·8°), □: t-ZrO_2; (2θ = 29·8°), ●: MgO; (2θ = 42·9°).

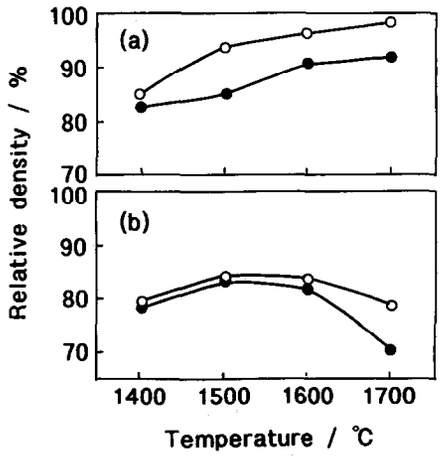

Fig. 8. Changes in the relative density of (a) MZ(6·64) compact and (b) MZ(24·49) compact with firing temperature. ●-●: as prepared powder compact, ○-○: wet-milled powder compact.

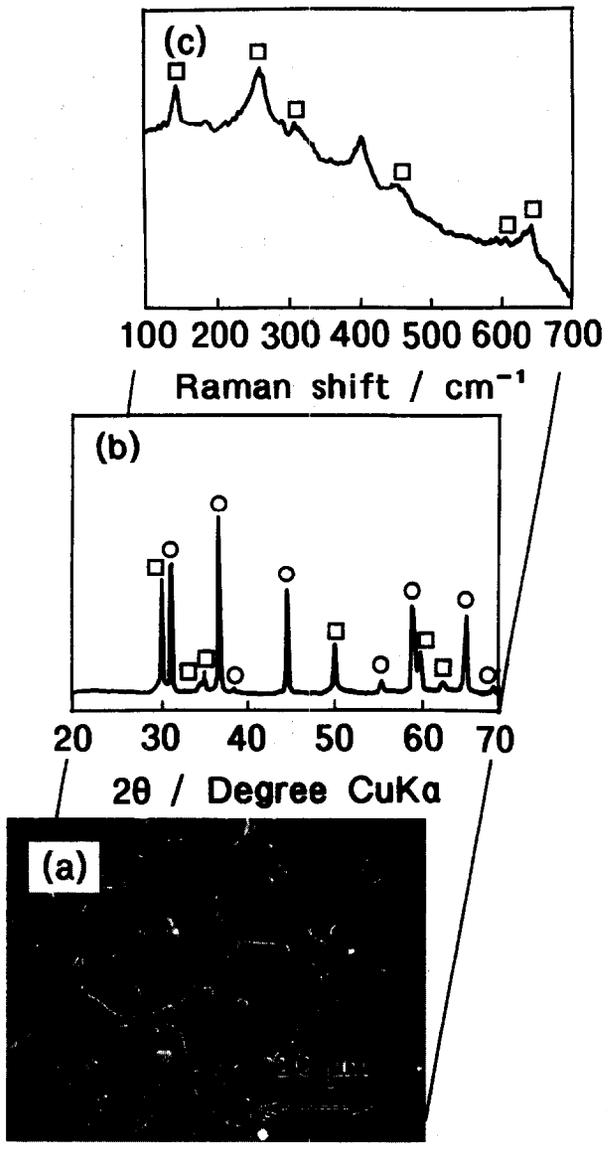

Fig. 9. (a) SEM micrograph, (b) XRD pattern and (c) Raman spectrum of the MZ(6.64) compact fired at 1700°C for 10 h. ○: $MgAl_2O_4$, □: t-ZrO_2, ●: MgO.

To check the crystalline phases of the large and small grains in the sintered body, EDX analysis was performed. Results are shown in Fig. 10. The elements Mg and Al were detected in the large polyhedral grains, whereas Zr and Y were detected in the small spherical grains. Thus the large polyhedral grains and small spherical grains correspond to $MgAl_2O_4$ and Y-TZP, respectively.

As shown above, Y-TZP grains are present not only on boundaries but also inside the $MgAl_2O_4$ grains. Since the mass transfer of $MgAl_2O_4$ is retarded by these Y-TZP grains present on grain boundaries, it cannot be promoted until Y-TZP grains are entrapped in the $MgAl_2O_4$ grains.

It is concluded from the present results that the double-nozzle ultrasonic spray pyrolysis technique is useful for preparing the composite powder without a mixing operation. By this technique, we can now examine the conditions for preparing many kinds of composite powders.

4 Conclusions

Spinel ($MgAl_2O_4$)-zirconia (ZrO_2) composite powders were prepared by the double nozzle ultrasonic spray pyrolysis technique. The results obtained are summarized as follows:

(1) The compositions of the composite powders were as follows: (1) Sample No. 1: $MgAl_2O_4$ 93·36 mol% and yttria-stabilized ZrO_2 polycrystals 6·64 mol% and (2) Sample No. 2: $MgAl_2O_4$ 75·51 mol% and Y-TZP 24·49 mol%. The powder compositions could be controlled by changing the flow rate of the carrier gas.

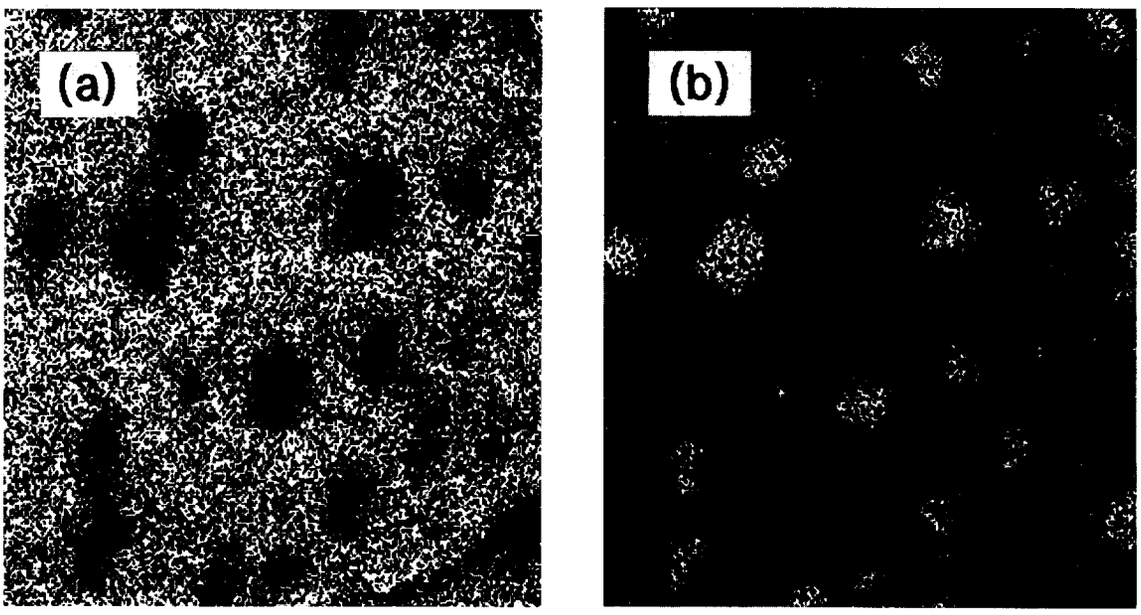

Fig. 10. EDX analysis of MZ(6.64) compact fired at 1700°C for 10 h. (a) MgKα and AlKα spectra, (b) ZrLα and YLα spectra.

(2) While $MgAl_2O_4$ and Y-TZP were present in both powders, MgO was additionally detected from Sample No. 2; such MgO disappeared when the powders were heated at and above 1100°C. The powders contained spherical particles with diameters of 2 μm.
(3) The wet-milled composite powder of Sample No. 1 showed excellent sinterability. When this powder compact was fired at 1700°C for 10 h, the relative density of the sintered compact attained 97·6%. The microstructural observation revealed that ZrO_2 grains were present not only on boundaries but also inside the $MgAl_2O_4$ grains.

Acknowledgements

The authors wish to express their thanks to Professor Dr T. Sekine and Ms T. Tanokura of Sophia University for Raman spectroscopic measurements and to Professor Dr Y. Toda and Dr Ka. Hashimoto of Chiba Institute of Technology for taking the TEM micrographs.

References

1. Alper, A. M., McNally, R. N., Ribbe, P. H. & Doman, R. C., The system MgO-$MgAl_2O_4$. *J. Am. Ceram. Soc.*, **45** (1962) 263–8.
2. Cooper, S. C. & Hodson, P. T. A., Magnesia-magnesium aluminate spinel as a refractory. *Br. Ceram. Trans. J.*, **81** (1982) 121–8.
3. Maschio, R. D., Fabbri, B. & Fiori, C., Industrial applications of refractories containing magnesium aluminate spinel. *Ind. Ceram.*, **8** (1988) 121–6.
4. Seiyama, T., Yamazoe, N. & Arai, H., Ceramic humidity sensors. *Sensors and Actuators*, **4** (1983) 85–96.
5. Shimizu, Y., Arai, H. & Seiyama, T., Theoretical studies on the impedance-humidity characteristics of ceramic humidity sensors. *Sensors and Actuators*, **7** (1985) 11–22.
6. Gusmano, G., Montesperelli, G., Traversa, E. & Mattogno, G., Microstructure and electrical properties of $MgAl_2O_4$ thin films for humidity sensing. *J. Am. Ceram. Soc.*, **76** (1993) 743–50.
7. Baudin, C., Martinez, R. & Pena, P., High-temperature mechanical behavior of stoichiometric magnesium spinel. *J. Am. Ceram. Soc.*, **78** (1995) 1857–62.
8. Fujita, M., Yoshimatsu, H., Osaka, A. & Miura, Y., Preparation and properties of ZrO_2-dispersed MgO-Al_2O_3 ceramic. *J. Ceram. Soc. Jpn*, **103** (1995) 81–4.
9. Bratton, R. L., Characterization and sintering of reactive $MgAl_2O_4$ spinel. *Am. Ceram. Soc. Bull.*, **48** (1969) 759–62.
10. Itatani, K., Sakai, H., Howell, F. S., Kishioka, A. & Kinoshita, M., Sinterability of spinel ($MgAl_2O_4$) powder prepared by vapour-phase oxidation technique. *Br. Ceram. Trans. J.*, **88** (1989) 13–16.
11. Kanzaki, S., Nishida, T., Otsuka, N., Saito, K., Nakagawa, Z. & Hamano, K., Sintering of spray pyrolysed Mg-Al spinel powder. *Yogyo-Kyokai-Shi*, **91** (1983) 24–30.
12. Nakagawa, Z., Hamano, K., Sakaguchi, M. & Kanzaki, S., Characterization and sinterability of Mg-Al spinel powders prepared with a thermal decomposition of a freeze-dried sulfate. *Yogyo-Kyokai-Shi*, **90** (1982) 312–19.
13. Lepkova, D., Batarjav, A., Samunevz, B., Ivanova, Y. & Georgieva, L., Preparation and properties of ceramics from magnesium spinel by sol-gel technology. *J. Mater. Sci.*, **26** (1991) 4861–4.
14. Itatani, K., Nishioka, T., Seike, S., Howell, F. S., Kishioka, A. & Kinoshita, M., Sinterability of β-calcium orthophosphate powder prepared by spray-pyrolysis. *J. Am. Ceram. Soc.*, **77** (1994) 801–5.
15. Itatani, K., Takahashi, O., Kishioka, A. & Kinoshita, M., Properties of hydroxyapatite prepared by spray-pyrolysis technique. *Gypsum & Lime*, No. 213 (1988) 19–27.
16. Aizawa, M., Itatani, K., Kishioka, A. & Kinoshita, M., Properties of calcium metaphosphate and calcium diphosphate powders prepared by spray-pyrolysis technique. *Gypsum & Lime*, No. 237 (1992) 22–30.
17. Messing, G. L., Zhang, S. C. & Jayanthi, G. C., Ceramic powder synthesis by spray pyrolysis. *J. Am. Ceram. Soc.*, **76** (1993) 2707–26.
18. Lang, R. J., Ultrasonic atomization of liquids. *J. Acoust. Soc. Am.*, **34** (1962) 6–8.
19. Powder Diffraction File Card No.21-1152, JCPDS International Center for Diffraction Data, Newtown Square, PA (1971).
20. Powder Diffraction File Card No. 24-1164, JCPDS International Center for Diffraction Data, Newtown Square, PA (1973).
21. Powder Diffraction File Card No. 4-0829, JCPDS International Center for Diffraction Data, Newtown Square, PA (1949).
22. Arai, Y. & Yasue, T., *Gypsum & Lime*, No. 187 (1983) 357–66.
23. Hamano, K., Nakagawa, Z. & Watanabe, H., Effects of magnesium compound additives on sintering of magnesia. In *Sintering—Theory and Practice*, ed. D. Kolar, S. Pejovni & M. M. Ristić. Elsevier Scientific Publishing Co., Amsterdam, 1981, pp. 159–64.
24. *Kagaku Daijiten*, Vol. **4**, Compiled by the Committee of Kagaku Daijiten, Kyoritsu Shuppan, Tokyo, Japan, 1979, p. 772.
25. *Kagaku Daijiten*, Vol. **2**, Compiled by the Committee of Kagaku Daijiten, Kyoritsu Shuppan, Tokyo, Japan, 1979, p. 39.
26. *Gmelin Handbook of Inorganic Chemistry*, ed. H. Bergmann. Springer Verlag, Berlin, 1982, pp. 43–4.
27. Itatani, K., Kishioka, A. & Kinoshita, M., Synthesis of starting powders for ceramics by spray-pyrolysis technique. *Gypsum & Lime*, No. 241 (1992) 25–34.
28. Matsumoto, R. L. K., Generation of powder compaction response diagrams. *J. Am. Ceram. Soc.*, **69** (1995) C-246–C-247.
29. Haberko, K., Characteristics and sintering behaviour of zirconia ultrafine powders. *Ceramurgia International*, **5** (1979) 148–54.
30. Phillippi, C. M. & Mazdiyasni, K. S., Infrared and Raman spectra of zirconia polymorphs. *J. Am. Ceram. Soc.*, **54** (1971) 254–8.